Research Article | Vol. 8, No. 4 | 1 Apr 2017 | BIOMEDICAL OPTICS EXPRESS 2173

Biomedical Optics EXPRESS

Three-dimensional OCT based guinea pig eye model: relating morphology and optics

Pablo Pérez-Merino,[1,*] Miriam Velasco-Ocana,[1] Eduardo Martinez-Enriquez,[1] Luis Revuelta,[2] Sally A McFadden,[3] and Susana Marcos[1]

[1]*Instituto de Óptica "Daza de Valdés", Consejo Superior de Investigaciones Científicas (CSIC), Madrid, Spain*
[2]*Facultad de Veterinaria, Universidad Complutense, Madrid, Spain*
[3]*School of Psychology, University of Newcastle, Newcastle, NSW, Australia*
[*]*p.perez@io.cfmac.csic.es*

Abstract: Custom Spectral Optical Coherence Tomography (SOCT) provided with automatic quantification and distortion correction algorithms was used to measure the 3-D morphology in guinea pig eyes (n = 8, 30 days; n = 5, 40 days). Animals were measured awake *in vivo* under cyclopegia. Measurements showed low intraocular variability (<4% in corneal and anterior lens radii and <8% in the posterior lens radii, <1% interocular distances). The repeatability of the surface elevation was less than 2 µm. Surface astigmatism was the individual dominant term in all surfaces. Higher-order RMS surface elevation was largest in the posterior lens. Individual surface elevation Zernike terms correlated significantly across corneal and anterior lens surfaces. Higher-order-aberrations (except spherical aberration) were comparable with those predicted by OCT-based eye models.

OCIS codes: (110.4500) Optical coherence tomography; (110.6880) Three-dimensional image acquisition; (100.2960) Image analysis; (330.7327) Visual optics, ophthalmic instrumentation; (330.7324) Visual optics, comparative animal models; (330.5370) Physiological optics.

References and links

1. D. O. Mutti, K. Zadnik, and A. J. Adams, "Myopia. The nature versus nurture debate goes on," Invest. Ophthalmol. Vis. Sci. **37**(6), 952–957 (1996).
2. E. Dolgin, "The myopia boom," Nature **519**(7543), 276–278 (2015).
3. F. Schaeffel and M. Feldkaemper, "Animal models in myopia research," Clin. Exp. Optom. **98**(6), 507–517 (2015).
4. M. H. Howlett and S. A. McFadden, "Form-deprivation myopia in the guinea pig (Cavia porcellus)," Vision Res. **46**(1-2), 267–283 (2006).
5. E. García de la Cera, G. Rodríguez, and S. Marcos, "Longitudinal changes of optical aberrations in normal and form-deprived myopic chick eyes," Vision Res. **46**(4), 579–589 (2006).
6. E. G. de la Cera, G. Rodríguez, A. de Castro, J. Merayo, and S. Marcos, "Emmetropization and optical aberrations in a myopic corneal refractive surgery chick model," Vision Res. **47**(18), 2465–2472 (2007).
7. N. J. Coletta, S. Marcos, and D. Troilo, "Ocular wavefront aberrations in the common marmoset Callithrix jacchus: effects of age and refractive error," Vision Res. **50**(23), 2515–2529 (2010).
8. P. Rosales, M. Wendt, S. Marcos, and A. Glasser, "Changes in crystalline lens radii of curvature and lens tilt and decentration during dynamic accommodation in rhesus monkeys," J. Vis. **8**(1), 1–12 (2008).
9. E. G. de la Cera, G. Rodríguez, L. Llorente, F. Schaeffel, and S. Marcos, "Optical aberrations in the mouse eye," Vision Res. **46**(16), 2546–2553 (2006).
10. H. E. Bowrey, A. P. Metse, A. J. Leotta, G. Zeng, and S. A. McFadden, "The relationship between image degradation and myopia in the mammalian eye," Clin. Exp. Optom. **98**(6), 555–563 (2015).
11. M. H. Howlett and S. A. McFadden, "Emmetropization and schematic eye models in developing pigmented guinea pigs," Vision Res. **47**(9), 1178–1190 (2007).
12. S. Ortiz, P. Pérez-Merino, E. Gambra, A. de Castro, and S. Marcos, "In vivo human crystalline lens topography," Biomed. Opt. Express **3**(10), 2471–2488 (2012).
13. P. Pérez-Merino, S. Ortiz, N. Alejandre, A. de Castro, I. Jiménez-Alfaro, and S. Marcos, "Ocular and optical coherence tomography-based corneal aberrometry in keratoconic eyes treated by intracorneal ring segments," Am. J. Ophthalmol. **157**(1), 116–127 (2014).
14. S. Ortiz, D. Siedlecki, I. Grulkowski, L. Remon, D. Pascual, M. Wojtkowski, and S. Marcos, "Optical distortion correction in optical coherence tomography for quantitative ocular anterior segment by three-dimensional imaging," Opt. Express **18**(3), 2782–2796 (2010).
15. S. Ortiz, D. Siedlecki, P. Pérez-Merino, N. Chia, A. de Castro, M. Szkulmowski, M. Wojtkowski, and S. Marcos, "Corneal topography from spectral optical coherence tomography (sOCT)," Biomed. Opt. Express **2**(12), 3232–3247 (2011).

#279913 https://doi.org/10.1364/BOE.8.002173
Journal © 2017 Received 2 Nov 2016; accepted 14 Feb 2017; published 15 Mar 2017
Corrected: 16 March 2017

Biomedical Optics EXPRESS

16. S. Ortiz, D. Siedlecki, L. Remon, and S. Marcos, "Optical coherence tomography for quantitative surface topography," Appl. Opt. **48**(35), 6708–6715 (2009).
17. P. Pérez-Merino, M. Velasco-Ocana, E. Martinez-Enriquez, and S. Marcos, "OCT-based crystalline lens topography in accommodating eyes," Biomed. Opt. Express **6**(12), 5039–5054 (2015).
18. S. Ortiz, P. Pérez-Merino, S. Durán, M. Velasco-Ocana, J. Birkenfeld, A. de Castro, I. Jiménez-Alfaro, and S. Marcos, "Full OCT anterior segment biometry: an application in cataract surgery," Biomed. Opt. Express **4**(3), 387–396 (2013).
19. E. Martinez-Enriquez, M. Sun, M. Velasco-Ocana, J. Birkenfeld, P. Pérez-Merino, and S. Marcos, "Optical Coherence Tomography Based Estimates of Crystalline Lens Volume, Equatorial Diameter, and Plane Position," Invest. Ophthalmol. Vis. Sci. **57**(9), 600–610 (2016).
20. I. Grulkowski, M. Gora, M. Szkulmowski, I. Gorczynska, D. Szlag, S. Marcos, A. Kowalczyk, and M. Wojtkowski, "Anterior segment imaging with Spectral OCT system using a high-speed CMOS camera," Opt. Express **17**(6), 4842–4858 (2009).
21. E. Martinez-Enriquez, P. Perez-Merino, M. Velasco-Ocana, and S. Marcos, "OCT-based full crystalline lens shape change during accommodation in vivo," Biomed. Opt. Express **8**(2), 918–933 (2017).
22. M. Sun, P. Pérez-Merino, E. Martinez-Enriquez, M. Velasco-Ocana, and S. Marcos, "Full 3-D OCT-based pseudophakic custom computer eye model," Biomed. Opt. Express **7**(3), 1074–1088 (2016).
23. S. R. Uhlhorn, D. Borja, F. Manns, and J. M. Parel, "Refractive index measurement of the isolated crystalline lens using optical coherence tomography," Vision Res. **48**(27), 2732–2738 (2008).
24. E. Moreno-Barriuso and R. Navarro, "Laser Ray Tracing versus Hartmann-Shack sensor for measuring optical aberrations in the human eye," J. Opt. Soc. Am. A **17**(6), 974–985 (2000).
25. R. Navarro and M. A. Losada, "Aberrations and relative efficiency of light pencils in the living human eye," Optom. Vis. Sci. **74**(7), 540–547 (1997).
26. S. Marcos, L. Díaz-Santana, L. Llorente, and C. Dainty, "Ocular aberrations with ray tracing and Shack-Hartmann wave-front sensors: does polarization play a role?" J. Opt. Soc. Am. A **19**(6), 1063–1072 (2002).
27. A. P. Lodge, and T. McFadden, SA, "Form deprivation myopia and emmetropization in the guinea pig," Proc Aust Neurosci Soc **5**, 123 (1994).
28. S. A. W. J. McFadden, "Guinea-pig eye growth compensates for spectacle lenses," Investigative Ophthalmology & Visual Science April 2011 Vol.52, 845. doi: **36**(4),S758 (1995).
29. S. A. McFadden, "Partial occlusion produces local form deprivation myopia in the guinea pig eye," Invest. Ophthalmol. Vis. Sci. **43**(13), 189 (2002).
30. M. H. Howlett and S. A. McFadden, "Spectacle lens compensation in the pigmented guinea pig," Vision Res. **49**(2), 219–227 (2009).
31. M. Sun, J. Birkenfeld, A. de Castro, S. Ortiz, and S. Marcos, "OCT 3-D surface topography of isolated human crystalline lenses," Biomed. Opt. Express **5**(10), 3547–3561 (2014).
32. M. Glickstein and M. Millodot, "Retinoscopy and eye size," Science **168**(3931), 605–606 (1970).
33. H. C. Howland, "Allometry and scaling of wave aberration of eyes," Vision Res. **45**(9), 1091–1093 (2005).
34. R. H. Kröger, "Optical plasticity in fish lenses," Prog. Retin. Eye Res. **34**, 78–88 (2013).
35. A. de Castro, S. Ortiz, E. Gambra, D. Siedlecki, and S. Marcos, "Three-dimensional reconstruction of the crystalline lens gradient index distribution from OCT imaging," Opt. Express **18**(21), 21905–21917 (2010).
36. J. Birkenfeld, A. de Castro, and S. Marcos, "Contribution of shape and gradient refractive index to the spherical aberration of isolated human lenses," Invest. Ophthalmol. Vis. Sci. **55**(4), 2599–2607 (2014).
37. A. de Castro, J. Birkenfeld, B. Maceo, F. Manns, E. Arrieta, J. M. Parel, and S. Marcos, "Influence of shape and gradient refractive index in the accommodative changes of spherical aberration in nonhuman primate crystalline lenses," Invest. Ophthalmol. Vis. Sci. **54**(9), 6197–6207 (2013).

1. Introduction

Newborn eyes are generally long-sighted, but during growth the eye balances optical changes with its increasing length to ultimately achieve emmetropia, in which during relaxed distance viewing, objects are well focused on the retina. In the presence of degraded image quality and/or hyperopic defocus the normal course of emmetropization is compromised and the eye continuous to grow in the axial dimension resulting in myopia [1]. Remarkably, the prevalence of myopia has increased in recent years, especially alarmingly in the developing economies of the East Asian area [2], making the identification of the etiology of myopia as well as the morphological and optical changes in the eye associated with myopia particularly important.

The use of animal models in myopia research (such as chickens, primates, tree shrews, guinea pigs or mice) allows testing the impact of manipulated visual experience on emmetropization and determination of the underlying mechanisms, as well as the effect of interventions [3]. Additionally, longitudinal studies of myopia development can occur within a much shorter time period than in humans. The guinea pig has been established as an effective myopia model, and stands as a common myopia model in Asian research labs today [4]. It is a mammal, shows a rapid ocular development, responds to lens-induced blur, is easy to raise and handle, and optical measurements are feasible. We have previously reported optical aberration measurements (using Hartmann

Biomedical Optics EXPRESS

Shack wavefront sensors) in other animal models, such as chickens [5, 6], marmosets [7], macaques [8] and mice [9]. However, despite the increasing use of the guinea pig model, and extensive research on the regulation of its eye growth (in terms of axial length and refractive error) [4, 10, 11], there is scarce information on its optical properties *in vivo*.

It is well accepted that emmetropization entails a fine tuning between the optical components and eye growth. As such, accurate knowledge of the ocular surface geometry and interocular distances are of interest. To date, all the data available in guinea pigs are limited to 1-dimentional axial distances *in vivo*, or 2-D geometric information from cross-sectional profiles from frozen sections in excised eyes. State-of-the art models of the guinea pig eye are based on that information [11].

Quantitative 3-D spectral Optical Coherence Tomography (sOCT) is very well suited to characterize the guinea pig eye in three dimensions, due to its superior resolution than other imaging modalities, high acquisition rates, and adequate lateral and axial range suitable for ocular dimensions. In previous works we have reported 3-D anterior segment biometry in human eyes *in vivo*, including anterior and posterior corneal and lenticular surface elevation maps [12–17], interocular distances along well identified axes [18] and full crystalline lens, beyond the margins of the pupil [19]. Quantitative analysis is possible by correction of distortions (fan, arising from the scanning architecture; optical, due to the refraction in the optical surfaces) and new automatic image processing algorithms that have allowed quantification.

In the current study, we applied a custom 3-D sOCT system to study the eye of the guinea pig animal model, and build eye models for this animal that can be used to explore relationships and tuning between the ocular components as well as to predict its optical properties. We specifically explored the relationships between the axes of astigmatism and higher-order surface irregularities across the different surfaces of the ocular components, and used eye's specific anatomical data to build computer eye models for the 30-40 day old guinea pig. This age corresponds to the time at which emmetropization has been previously reported to be completed [11]. A comparison with refraction and aberrometry data obtained in the same eyes allowed identifying the morphological contributing factors to refractive error and optical aberrations in the guinea pig eye, as well as other parameters potentially needed in the eye model, such as the gradient index distribution in the crystalline lens.

2. Material and methods

2.1. Animals and experimental design

Four pigmented guinea pigs (*Cavia porcellus*) aged at 30 (8 eyes) and 40 days (5 eyes) were used in the experiment. Wild-type animals were obtained from a farm (to guarantee that the strain did not suffer from inbreeding, which has been associated with ocular problems in laboratory animals) and raised in a 12/12 h light/dark cycle in the animal facility of the Facultad de Veterinaria, Universidad Complutense, Madrid, Spain (FV-UCM). Protocols were approved by the FV-UCM Ethical Committee and conformed to the ARVO statement for the Use of Animals in Ophthalmic and Vision Research. All measurements (Refraction, OCT and Laser Ray Tracing) were performed with the animal awake and under cycoplegia (induced by topical application of 1% cyclopentolate hydrochloride, Alcon Cusí, Barcelona, Spain). Prior to the measurement, the awake guinea pig was wrapped in a cloth capsule and placed in a cradle with the head and eyes exposed, and maintained as such during the measurements.

2.2. Refractive error

Refractive error was measured by streak retinoscopy (Welch Allyn, white light source) approximately 1.25 hrs after the application of cyclopegia, and in the absence of a pupil response. Refractive error was reported as the mean of the horizontal and vertical meridian. Additional estimates of refractive error were obtained from LRT (section 2.5) and OCT-based geometrical measurements (section 2.4).

Biomedical Optics EXPRESS

2.3. OCT system

The custom sOCT instrument, and a set of algorithms for automatic image processing and distortion correction (fan and optical) allowing quantification of the anterior and posterior corneal and crystalline lens topographies, interocular distances and lens shape have been described in detail in previous publications [15, 20]. Briefly, the set-up was based on a fiber-optics Michelson interferometer configuration with a superluminiscent diode (λ_0 = 840 nm, $\Delta\lambda$ = 50 nm) as a light source, and a spectrometer consisting of a volume diffraction grating and a CMOS camera as a detector. The effective acquisition speed was 25000 A-Scans/s. The axial range was 7 mm in depth, resulting in a theoretical pixel resolution of 3.4 µm. The nominal axial resolution, as given by the coherence length of the source, was 6.9 µm in tissue.

Measurements were collected in an 8x8 mm area and consisted of a collection of 50 B-scans each composed of 300 A-scans. The total acquisition time of a 3-D data set was 0.6 seconds. Three sets of 3-D images were captured sequentially: cornea, anterior lens, posterior lens and retina. 3-D cornea and crystalline lens sets of data contained the iris to facilitate further merging. The specular reflection of the posterior crystalline lens surface was also used to merge the retina.

2.4. OCT image processing, anterior segment quantification and OCT-ocular wave aberrations

In previous studies in humans, we described image-processing tools for distortion correction using 3-D ray tracing routines, surface segmentation and merging of volumes, and we showed the 3-D anterior segment (cornea and crystalline lens) quantification capabilities of our methodology for corneal and crystalline lens surface and axial distances characterization [17] and lens shape estimation (volume (VOL), diameter (DIA), equatorial plane position (EPP), and lens surface area (LSA)) [19, 21]. Modifications of the routines were required to adapt the algorithms to the dimensions and signal properties of the guinea pig eye, especially due to the following challenging conditions: (1) the tilted anatomy of the guinea pig eyes, (2) the proximity of the corneal surfaces, (3) the tilted iris (particularly in the vertical meridian) and (4) the removal of the ghost retinal image (which appeared in the central area of the crystalline lens).

The geometrical axial distances between ocular surfaces taken from the apex position were: corneal thickness, anterior chamber depth (ACD), lens thickness and vitreous chamber depth (VCD). Corneal and lens surfaces were fitted by (1) spheres, described by the radii of curvature, (2) conicoids, described by the radii of curvature and asphericity, and (3) Zernike polynomial expansions (4th order; note that these Zernike coefficients describe surface elevations, not wave aberrations) of the surface elevation maps (relative to the best fitting sphere), described by individual Zernike coefficients. Surface elevation maps were given for the largest common aperture across surfaces (2-mm diameter, limit fixed by the posterior lens surface after distortion correction).

Ocular wave aberrations were estimated from ray tracing analysis on the OCT-based ocular surfaces [13, 22]. The ocular surfaces were exported to ZEMAX (Radiant ZEMAX, Focus software, Tucson, Arizona, USA). Matlab (MathWorks, Natick, MA) was used to create a suitable input file into ZEMAX DDE toolbox. Refractive indices of 1.376, 1.3346 and 1.401 were used for the cornea, aqueous-vitreous humor and crystalline lens, respectively [11]. The refractive index of the crystalline lens was calculated from an *ex vivo* guinea pig crystalline lens using the method proposed by Uhlhorn et al. [23]. Wave aberrations were calculated by tracing an array of 64x64 collimated IR-light beams (786 nm, same as Laser Ray Tracing) within 2-mm pupil diameter area through 4-surfaces (cornea and crystalline lens).

Figure 1 shows an example of the image processing from the acquisition of 3-D data set collected at different depths to the final quantification results after distortion correction.

Biomedical Optics EXPRESS

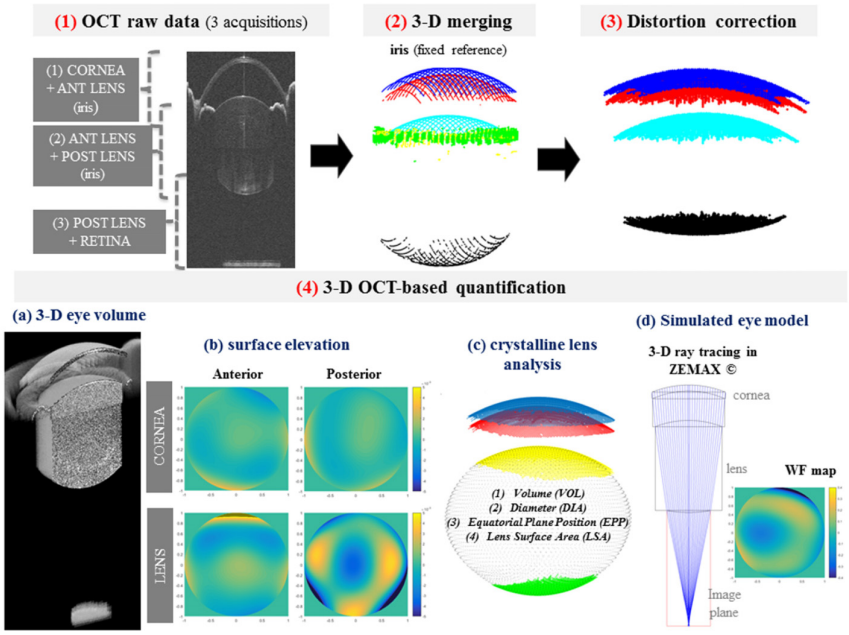

Fig. 1. Illustration of the image processing and quantification algorithm: (1) three acquisitions of cornea, crystalline lens and retina images; (2) merging of segmented anterior segment volumes (cornea and crystalline) by using the pupil as fixed reference to obtain a 3-D full volume; (3) corneal and crystalline lens surfaces corrected from fan and optical distortion; (4) Quantification: (a) 3-D model eye, (b) quantitative elevation maps (elevation maps represent only the high-order coefficients), (c) full shape reconstruction of the crystalline lens, and (d) wavefront computation in ZEMAX by tracing rays through 3-D corneal and lens surfaces (WF map represents the HOAs).

2.5. Laser Ray Tracing (LRT): total wave aberration measurements

Total wave aberrations were measured in four guinea pig eyes (at 30 days) using a custom Laser Ray Tracing (LRT) aberrometer, described in detail in previous studies [24–26]. The sampling pattern was adjusted to fit a 4-mm pupil diameter in the guinea pig animal model. An IR (785 mm) laser beam sequentially sampled 37 pupil positions in a hexagonal pattern in 1.5 seconds. Ray aberrations were obtained by estimating the deviations of the centroids of the retinal spots images corresponding to each entry pupil position with respect to the reference (chief ray). Figure 2 shows the LRT illustration on a guinea pig eye.

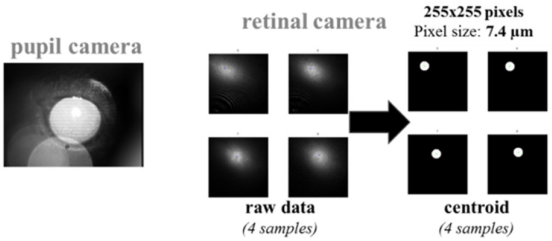

Fig. 2. LRT measurement illustration on a guinea pig eye. Left: Back illuminated pupillary image collected in pupil camera. Right: example of 4 retinal images and the corresponding centroid position of the retinal spots.

2.6. Optical quality metrics

Wave aberrations were described in terms of individual Zernike coefficients or Root Mean Square (RMS). RMS was used to report the magnitude of high-order aberrations (HOAs) and certain relevant aberrations. The Point-Spread-Function (PSF) and the

Biomedical Optics EXPRESS

Modulation Transfer Function (MTF) were computed by means of Fourier optics routines written in Matlab.

3. Results

3.1. Refractive error

The spherical equivalent refractive error of the animals measured by streak retinoscopy under cycloplegia was 1.414 ± 0.62 D (mean ± standard error). Photoretinoscopy results matched well with LRT and eye model ray tracing estimates based on the defocus Zernike term (LRT (Z_2^0): 2.48 ± 1.18 D; OCT (Z_2^0): 0.92 ± 0.56 D). On average, the paraxial refractive equivalent power based on the OCT radii of curvature was 129.4 ± 2.9 D (crystalline lens: 44.5 ± 1.4 D) at 30 days, and 126.5 ± 2.4 D (crystalline lens: 44.8 ± 1.2 D) at 40 days.

3.2. 3-D biometry, lens analysis and corneal/crystalline lens surface elevation maps

Figure 3 (Visualization 1) shows an example of the corneal and crystalline lens segmented surfaces from OCT and the corresponding axial and geometric data (left), the parameters of the crystalline lens whole shape (right, top) and the anterior segment surface elevation maps including astigmatism and high-order Zernike coefficients (right, bottom; 2-mm pupil diameter).

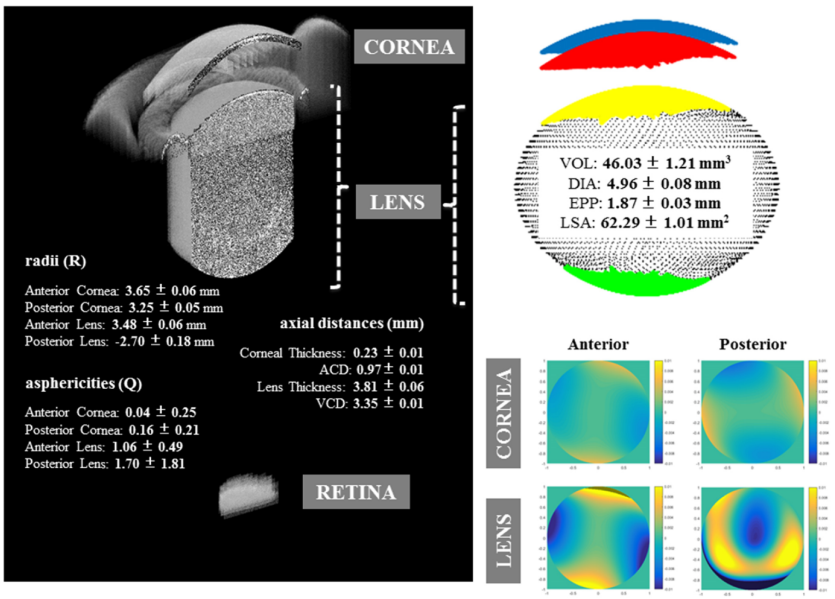

Fig. 3. (Visualization 1). Example of the OCT analysis on a guinea pig eye at 30 days. Left: 3-D view of the merged whole guinea pig eye (cornea, crystalline lens and retina) and the corresponding geometrical and biometrical data. Right: volume (VOL, in mm^3), diameter (DIA, in mm), equatorial plane position (EPP, in mm), lens surface area (LSA, in mm^2) and the surface elevation maps (maps represent astigmatism and high-order coefficients). Data are shown as mean ± standard deviation.

Table 1 shows average results at 30 and 40 days of anterior and posterior corneal and crystalline lens geometry (radius of curvature, from best-fit sphere and conic; and asphericity), axial distances (corneal and lens thicknesses, ACD and VCD) and 3-D crystalline lens analysis (VOL, DIA, EPP and LSA). Although all geometrical and biometrical parameters are higher at 40 days, only 3-D crystalline lens shape parameters (VOL, EPP and LSA) were, on average, statistically significantly higher with age ($p < 0.05$). Intra-ocular repeatability in the estimated radii of curvature, axial distances and crystalline lens shape estimation is high, with average standard deviations of

Biomedical Optics EXPRESS

0.05/0.04/0.05/0.11 mm (Radii: anterior cornea/posterior cornea/anterior lens/posterior lens), 0.0003/0.002/0.04/0.01 mm (axial distances: corneal thickness/ACD/lens thickness/VCD) and 0.87 mm^3/0.04 mm/0.03 mm/0.56 mm^2 (VOL/DIA/EPP/LSA).

Table 1. Biometrical and geometrical properties for the five corresponding eyes at 30 and 40 days (average ± SD; R, axial distances, DIA and EPP in mm; VOL in mm^3 and LSA in mm^2). *represents statistically significant ($p<0.05$).

		30 days	40 days
R (sphere)	*Anterior Cornea*	3.57 ± 0.14	3.65 ± 0.06
	Posterior Cornea	3.26 ± 0.03	3.30 ± 0.11
	Anterior Lens	3.28 ± 0.13	3.23 ± 0.19
	Posterior Lens	–2.47 ± 0.21	–2.49 ± 0.13
R (conic)	*Anterior Cornea*	3.59 ± 0.15	3.68 ± 0.06
	Posterior Cornea	3.26 ± 0.05	3.27 ± 0.22
	Anterior Lens	3.41 ± 0.19	3.30 ± 0.21
	Posterior Lens	–2.73 ± 0.17	–2.85 ± 0.23
Q	*Anterior Cornea*	–0.45 ± 0.82	0.01 ± 0.27
	Posterior Cornea	–0.29 ± 0.94	0.09 ± 0.38
	Anterior Lens	0.84 ± 0.80	–0.09 ± 0.74
	Posterior Lens	0.50 ± 1.49	2.77 ± 1.13
Corneal Thickness		0.23 ± 0.005	0.23 ± 0.006
ACD		0.99 ± 0.02	1.01 ± 0.02
Lens Thickness		3.79 ± 0.14	3.96 ± 0.09
VCD		3.35 ± 0.03	3.40 ± 0.04
VOL(Crystalline lens)		45.10 ± 2.56*	49.64 ± 1.25*
DIA (Crystalline lens)		4.92 ± 0.08	5.02 ± 0.06
EPP (Crystalline lens)		1.86 ± 0.05*	1.94 ± 0.02*
LSA (Crystalline lens)		61.32 ± 2.26*	65.04 ± 1.21*

Table 2 shows average RMS of astigmatism, HOAs, coma, trefoil and the spherical Zernike term at 30 and 40 days for all surface elevation (cornea and crystalline lens; data are for 2-mm pupil diameter). Figure 4 shows the corresponding Zernike terms and surface lens elevation maps.

Table 2. RMS of the anterior segment surfaces at 30 and 40 days (average ± SD, µm)

		30 days	40 days
RMS Astigmatism	*Anterior Cornea*	3.39 ± 3.20	2.03 ± 0.47
	Posterior Cornea	2.08 ± 1.01	1.14 ± 0.67
	Anterior Lens	6.30 ± 2.58	5.34 ± 0.45
	Posterior Lens	5.26 ± 2.19	2.92 ± 1.21
RMS HOAs	*Anterior Cornea*	0.60 ± 0.13	0.58 ± 0.14
	Posterior Cornea	0.72 ± 0.32	0.59 ± 0.07
	Anterior Lens	1.42 ± 0.46	1.19 ± 0.36
	Posterior Lens	5.24 ± 2.69	5.38 ± 0.64
RMS Coma	*Anterior Cornea*	0.34 ± 0.17	0.32 ± 0.19
	Posterior Cornea	0.49 ± 0.22	0.44 ± 0.14
	Anterior Lens	1.01 ± 0.40	0.83 ± 0.34
	Posterior Lens	3.78 ± 3.06	3.83 ± 0.41
RMS Trefoil	*Anterior Cornea*	0.28 ± 0.16	0.28 ± 0.16
	Posterior Cornea	0.33 ± 0.32	0.18 ± 0.06
	Anterior Lens	0.60 ± 0.46	0.50 ± 0.32
	Posterior Lens	1.62 ± 0.59	1.54 ± 0.40
Spherical	*Anterior Cornea*	0.26 ± 0.12	0.28 ± 0.03
	Posterior Cornea	0.32 ± 0.05	0.31 ± 0.07
	Anterior Lens	0.62 ± 0.08	0.56 ± 0.04
	Posterior Lens	–1.94 ± 1.28	–2.86 ± 0.63

Biomedical Optics EXPRESS

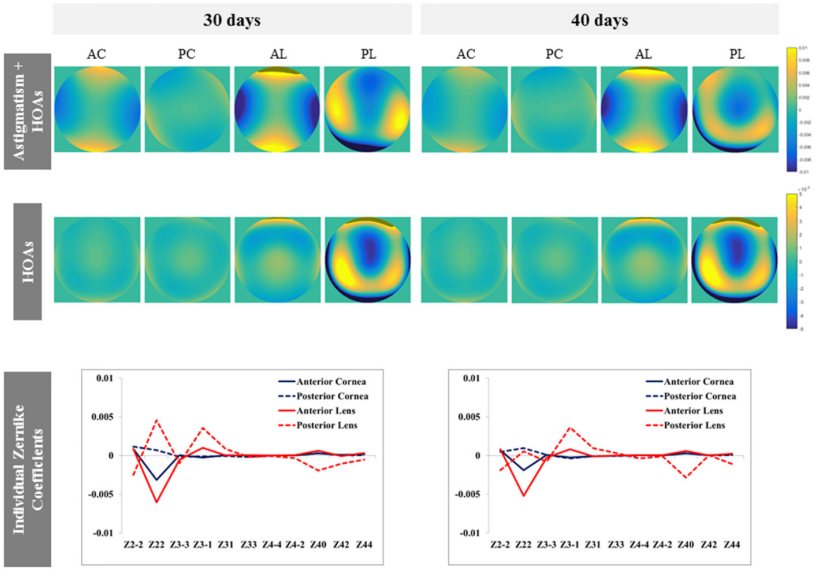

Fig. 4. Anterior and posterior corneal and crystalline lens surface elevation maps at 30 and 40 days (astigmatism and HOAs: maps exclude tilt and defocus; HOAs: maps exclude tilt, defocus and astigmatism. Scale bar range in mm).

Surface elevation RMS intraocular repeatability was: 0.14/0.13 µm (anterior cornea), 0.32/0.07 µm (posterior cornea), 0.46/0.36 µm (anterior lens) and 2.69/0.64 µm (posterior lens) at 30/40 days, respectively. The higher corneal coefficients were H/V astigmatism (Z_2^2; anterior cornea: 64-53%, posterior cornea: 25-38% for 30-40 days) and oblique astigmatism (Z_2^{-2}; anterior cornea: 17-19%, posterior cornea: 42-19% for 30-40 days), followed by spherical (Z_4^0; anterior cornea: 5-8%, posterior cornea: 12-13% for 30-40 days) and vertical coma (Z_3^{-1}; anterior cornea: 5-7%, posterior cornea: 5-15% for 30-40 days). The higher lens coefficients were H/V astigmatism (Z_2^2; anterior lens: 63-64%, posterior lens: 27-4% for 30-40 days) and oblique astigmatism (Z_2^{-2}; anterior lens: 9-10%, posterior lens: 15-15% for 30-40 days), followed by spherical (Z_4^0; anterior lens: 6-7%, posterior lens: 12-23% for 30-40 days) and vertical coma (Z_3^{-1}; anterior lens: 10-10%, posterior lens: 21-29% for 30-40 days).

The magnitude of astigmatism in the anterior lens was x2.24, x3.85 and x1.51 times higher in comparison with the astigmatism of the anterior cornea, posterior cornea and posterior lens, respectively. The RMS of coma of the posterior crystalline lens surface was more than 5 times higher in comparison with corneal and anterior lens surfaces. The H/V astigmatism (Z_2^2) is the only Zernike coefficient that showed a marked opposite sign between corneal surfaces. The sign of anterior and posterior crystalline lens surfaces was markedly opposite in both astigmatism coefficients (oblique and H/V) and in the spherical term. Corneal and lens elevation maps at 30 and 40 days generally showed a similar shape, although there was a statistically significant ($p<0.05$) decrease in astigmatism and some higher-order irregularities in the crystalline lens at 40 days (anterior lens: Z_3^3 x9, Z_4^2 x29; posterior lens: Z_2^2 x9, Z_4^2 x39).

Table 3. Pearson correlation coefficient and p-value between corneal and lens surfaces at 30 and 40 days (average of eyes)

	30 days		40 days	
	Astigmatism + HOAs	HOAs	Astigmatism + HOAs	HOAs
Cornea (Anterior vs Posterior)	r=-0.18; p=0.58	r=0.73; p=0.02*	r=-0.49; p=0.11	r=0.95; p<0.001*
Anterior Cornea vs Anterior Lens	r=0.95; p<0.001*	r=-0.28; p=0.45	r=0.93; p<0.001*	r=-0.08; p=0.82
Crystalline Lens (Anterior vs Posterior)	r=-0.63; p=0.03*	r=0.52 ; p=0.15	r=-0.12; p=0.7	r=0.24; p=0.52

Biomedical Optics EXPRESS

Table 3 shows the correlations between anterior segment surface terms (cornea and crystalline lens). A significant correlation indicates that the magnitudes of individual Zernike terms of the surfaces are closely associated. We found a strong positive correlation between the higher-order coefficients of the corneal surfaces and between the anterior cornea and the anterior lens surfaces (for both astigmatism and higher-order coefficients).

3.3. Wave aberrations: simulation (OCT) vs experimental (LRT)

OCT and LRT ocular aberrations were compared in 4 eyes. Figure 5 shows the corresponding wave aberration maps (A. top: LRT, bottom: OCT; B. Higher-order Zernike coefficients; for 2-mm pupil diameter). The lack of knowledge of the fixation axis in the guinea pig eyes has prevented us from a comparative astigmatism analysis (RMS astigmatism: LRT, 0.23 ± 0.06 µm; OCT, 0.56 ± 0.20 µm). RMS for HOAs was 0.10 ± 0.04 µm and 0.18 ± 0.04 µm from LRT and OCT-based simulations. A marked shift between LRT and OCT was observed in the spherical aberration (on average, Z_4^0: –0.02 ± 0.06 µm from LRT; + 0.04 ± 0.02 µm from OCT), suggesting the presence of the gradient index (GRIN) distribution in the crystalline lens.

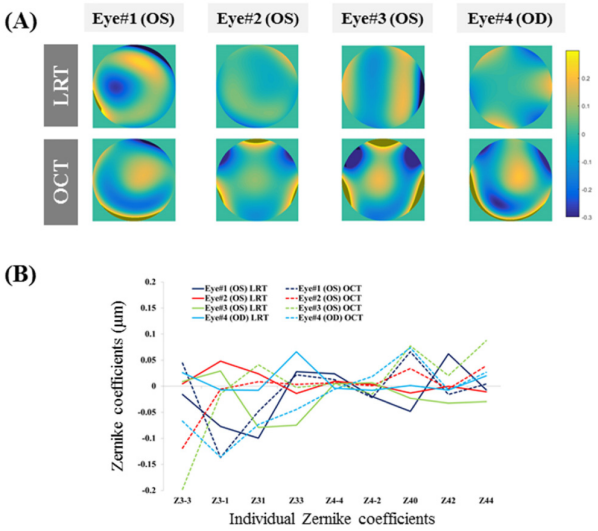

Fig. 5. A. LRT (experimental) and OCT (simulation) ocular aberration wavefront maps for 4 different eyes (HOAs: maps exclude tilt, defocus and astigmatism). B. Corresponding wave high-order Zernike terms. Data are for 2-mm pupil diameter.

3.4. Modulation Transfer Function (MTF)

Figure 6 shows a comparison of calculated (OCT, guinea pig) and measured (LRT, guinea pig and human) MTFs for 2-mm pupil diameter, considering only high-order aberrations. For comparison purposes with previous studies on mice eyes, we also calculated the MTF for 1.5-mm pupil at 2 c/deg: 0.95 for high-order aberrations only.

Biomedical Optics EXPRESS

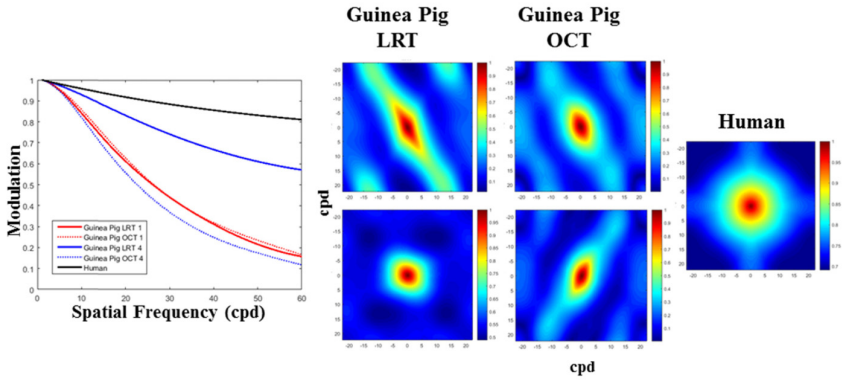

Fig. 6. One-dimensional (graph) and two-dimensional (colour panel) modulation transfer function (MTFs) for high-order aberrations in two guinea pig eyes (LRT and OCT; top: eye#1, bottom: eye#4) and one human eye (LRT). Data are for 2-mm pupils.

4. Discussion

The guinea pig is an increasingly used model for myopia since it was first introduced in 1994/95 [27, 28]. The guinea pig develops deprivation myopia in a short period of time [4] with independent growth in different retinal hemifields [29] and responds to lens-induced blur [30].

Despite the widespread use of the model, current *in vivo* biometric data on the guinea pig eye are limited primarily to axial biometry and there is little knowledge about its optical quality, with information about surface curvatures limited to that based on anatomical estimates from frozen eye sections [11].

Development of eye models for the guinea pig, relating biometric and optical information is critical to understanding the emmetropization process, the relative contribution of the cornea and lens to optical quality, and the magnitude and distribution of optical aberrations in the guinea pig eye. Analysis using these eye models will help answer questions that are relevant to the mechanisms for emmetropization, the understanding of the interplay between the eye's anatomical and optical changes occurring during myopia development, and to assess the impact of potential of myopia treatments.

In this study we report quantitative OCT 3-D geometry of the anterior segment of the eye in the guinea pig (ages 30 and 40 days), biometry, aberrometry and refractometry, which allowed us to develop 3-D OCT-based model eyes of the guinea pig eye and connect morphological and optical properties in these eyes. We have previously used custom spectral OCT provided with automatic quantitative image processing and distortion correction algorithms to characterize the anterior segment of the human eye in 3-D, including reconstruction of the crystalline lens full shape (beyond the iris). Unlike in humans, where the sensitivity drop-off of spectral OCT is insufficient to image the vitreous chamber depth, the smaller dimension of the guinea pig eye has allowed imaging the posterior crystalline lens and the retina in the same image captures and therefore same-instrument based eye models. In a previous study, we found an excellent match between the optical aberrations measured with LRT and those simulated using OCT-based custom eye models in pseudophakic patients [22]. Such comparisons in guinea pigs will allow the assessment of the potential contributions of the cornea and lens to retinal image quality and potential contributions of the crystalline lens gradient-index (GRIN).

The measured axial distances and radii of curvature of the cornea and crystalline lens surfaces are comparable to values in the literature at 30 days [11]: 8.26 [11] / 8.37 [our study] mm reported axial length and 3.54 [11] / 3.57 [our study] of anterior corneal radius of curvature *in vivo*, and 3.06 [11] / 3.28 [our study], –2.36 [11] / –2.47 [our study] mm of anterior-posterior crystalline lens radii of frozen eye sections *ex vivo*. The 3-D and higher resolution nature of the OCT system allowed robust estimates of surface radii of curvature, which showed low intra-ocular variability (standard deviations on average

Biomedical Optics EXPRESS

across repeated measurements and surfaces: 0.06 mm, radii; less than 0.02 mm, axial distances; and less than 2 µm, RMS of the surfaces), and low inter-animal variability (standard deviations on average across animals and surfaces: 0.11 mm, radii; less than 0.04 mm, axial distances; and less than 3 µm, RMS of the surfaces). The guinea pig eyes showed highly curved corneal and crystalline lens refracting surfaces. We found that the greatest proportion of the eye's power (65%) was due to the cornea, although the crystalline lens played a significant role in the eye's high order aberrations. As found in humans using OCT-based crystalline lens topography both *ex vivo* [31] and *in vivo* [12, 17], we found that the astigmatism of the anterior and posterior lens tends to be crossed, and higher amounts of surface irregularities in the posterior lens.

We found a relative good match between the spherical error measured with streak retinoscopy, Laser Ray Tracing and virtual ray tracing on the 3-D OCT custom eye model. Discrepancies (around 1 D) likely arise from the difference in wavelength (white light in retinoscopy and IR in OCT), the small eye [32] and associated uncertainty in the retinal layer in which reflection takes place. Also, predictions of optical power from optical models are affected by the assumed index of refraction, particularly for the lens which occupies a large fraction of the guinea pig eye. We used a measured crystalline lens refractive index of 1.401, lower from a previous reported value of 1.564 [11] or others reported in other species (i.e. 1.444 in mice [9]). We did not attempt to estimate refractive astigmatism from eye models, as this is significantly affected by the fixation angle. Our human custom OCT-based eye models incorporate angle lambda obtained by documenting the eye's fixation angle that allows alignment of the optical axis of the instrument with the pupillary axis of the eye (which results in a flat view of the iris in the horizontal and vertical preview B-scans [17, 21]). OCT images in the guinea pig were acquired at an angle such that allowed a flat view of the iris in the horizontal (but not the vertical preview) as the alignment of the animal is challenging, although highly repetitive results were found. The high amounts of astigmatism found in the anterior and posterior crystalline lens surfaces may arise from a non-physiological alignment, and differences in the centration of the lens in the horizontal and vertical axis. We found that off-axis ray tracing on the custom eye model could modify the estimated astigmatism by 2 D with a change of 5-13 deg in the angle of incidence. On the other hand, aberrometric refractive astigmatism (–2.32 ± 0.64 D) matches well that obtained from streak retinoscopy (–1.07 ± 0.41 D), indicating that the eye's fixation may have been similar in both types of measurements.

Previous reports [10, 11] have investigated biometric longitudinal changes in the guinea pig eye, over a longer period than in our study. We found an increase in lens thickness (~150 µm) and a statistically significant increase in lens volume (4.5 mm^3) and lens surface area (1.9 mm^2), which is consistent with the previously reported increase of 105 µm between 30 and 40 days of age [11] and it is indicative of consistent lens growth. The fact that the shape of the ocular surfaces (including pattern of higher order irregularities) remains almost constant between measurements 10-days apart suggests a coordinated growth of the ocular components. Although small, we found a decrease of high-order irregularities in the crystalline lens (particularly, astigmatism coma and trefoil) with age. A decrease of aberrations (coma in particular) occurs in chicks during the emmetropization process [5, 33], suggesting a geometrically driven decrease in aberrations. The fact that, for the same pupil diameter, optical quality decreases during eye development does not necessarily imply a decrease in the optical aberrations, but may result from the age-related geometrical changes.

The optical quality of the guinea pig eye largely exceeds that of the mouse [9] but remains similar to that of the chicken eye [5]. For 1.5 mm pupils (a pupil of reference in previous studies on these animal models [9], the MTF at the spatial frequency 2 c/deg was >0.9 in the guinea pig (considering HOAs), ~0.5 in mice and >0.9 in chickens. Although the numerical aperture differs across those eyes (NA = 0.5 in the mouse, 2.6 in the chicken and 2.4 in the guinea pig), the large difference suggests more highly contrasted images in the guinea pig than in mouse. This finding is consistent with the

Biomedical Optics EXPRESS

relatively higher estimated acuity in the guinea pig compared to the mouse (guinea pig: 2.4 – 2.7 c/deg [10], mouse: 0.5-0.6 c/deg [9]).

A comparison of the LRT and OCT-based measures (Fig. 5) revealed a sign reversal in the spherical aberration term. In our computations we have assumed a constant index of refraction in the crystalline lens. However, the presence of a gradient index profile in the lens would in fact be consistent with this finding. A compensatory role of the gradient in crystalline lens has been reported in fish [34], porcine lenses [35] and young lenses [36, 37]. Further estimates of the crystalline lens GRIN profile will be enabled by inverse modeling from OCT data of the lens collected in two orientations (anterior lens up and posterior lens up) *ex vivo*. These estimates will allow a direct test of the role of the GRIN, and confirm the origin of the apparent discrepancy.

In summary, 3-D OCT is a reproducible technique to evaluate *in vivo* and without any potential complications of anesthesia, the full 3-D anterior segment shape and to further explore the source of optical aberrations allowing quantitative eye models relating morphology and optics in animal models for myopia.

Funding

European Research Council under the European Union's Seventh Framework Program (FP/2007-2013) / ERC Grant Agreement [ERC-2011-AdC- 294099]. Spanish Government grant FIS2011-25637 and FIS2014-56643-R to SM. HRMI/UN grants to SAM.